Research Square

Preprints are preliminary reports that have not undergone peer review.
They should not be considered conclusive, used to inform clinical practice,
or referenced by the media as validated information.

MB degradation under UV–Vis using ZnO-Fe2O3@SiO2 monolithic filters in a CPC reactor

A. S. Galindo-Luna
Universidad Autónoma de Nuevo León (UANL)
I. Juárez-Ramírez
isaias.juarezrm@uanl.edu.mx
Universidad Autónoma de Nuevo León (UANL)
M. E. Zarazúa-Morín
Universidad Autónoma de Nuevo León (UANL)
D. Sánchez-Martínez
Universidad Autónoma de Nuevo León (UANL)
V. J. Gallegos-Sánchez
Universidad Tecnológica General Mariano Escobedo

Research Article

Keywords: Silica filters, ZnO-Fe2O3@SiO2, CPC reactor, Photocatalysis, Methylene blue

Posted Date: May 13th, 2026

DOI: https://doi.org/10.21203/rs.3.rs-9683860/v1

License: This work is licensed under a Creative Commons Attribution 4.0 International License.
Read Full License

Additional Declarations: No competing interests reported.

Abstract

It is reported the use of ZnO-Fe_2O_3@SiO_2 monolithic filters to the degradation of methylene blue (MB) under UV-Vis light irradiation in a CPC reactor. ZnO-Fe_2O_3@SiO_2 monolithic filters were obtained by deposition of ZnO and α-Fe_2O_3 particles on monolithic silica filters through hydrothermal method. Structural analysis by X-ray diffraction (XRD) showed the presence of ZnO and SiO_2 phases, corroborated by Scanning Electron Microscopy (SEM) coupled with Energy-Dispersive X-ray Spectroscopy (EDS), where chemical composition also detected a low percentage of Fe. Likewise, by X-ray Photoelectron Spectroscopy (XPS) the oxidation state of the elements presented in all phases was detected. Results exhibited that ZnO and Fe_2O_3 particles are homogeneously deposited and distributed on the silica surface to promote oxidation-reduction reactions during the degradation process. Photocatalytic activity of ZnO-Fe_2O_3@SiO_2 monolithic filters used in a CPC photocatalytic reactor for the degradation of methylene blue (MB) achieved 95% efficiency remaining intact after three reaction cycles, reaching also a high mineralization reaction (66%). The proposal mechanism indicates that the high generation of oxidizing species (peroxide and hydroxyl radicals), provoked by the presence of the deposited ZnO and α-Fe_2O_3 semiconductors, causes the breaking of the bonds of the dye until mineralization. In conclusion, ZnO-Fe_2O_3@SiO_2 monolithic filters here reported are presented as an innovative alternative for their application to degrade methylene blue dye in a CPC photocatalytic reactor for water treatment, due to its easy preparation, practicality and recyclability.

1. INTRODUCTION

In recent decades there has been increased concern about the presence of emerging pollutants in wastewater due to possible health effects as endocrine disruptors, antiandrogens capable of creating microbiological resistivity or producing metabolic alterations in humans, while in aquatic organisms they may have a cumulative effect and sex change [1–3]. This problematic is because many of these organic compounds are highly stable, biodegradation-resistant, and water-soluble species. Synthetic dyes are widely used in the textile, paper, leather, plastic, printing, and cosmetic industries, so effluent with a small amount of these dyes can cause serious local environmental problems [4]. Heterogeneous photocatalysis is presented as a viable option for the degradation of organic pollutants due to its capacity to produce drastic changes in the structure of the contaminant due to the generation of oxidative species that achieve the mineralization of the molecule [5–7]. Photocatalysts are commonly used as powders suspended in solution for their practicability [8]. However, some problems are present during their use such as a low and inherent surface area, limited adsorption capacity, secondary contamination and difficulties in scaling up processes and recyclability [9–10]. To mitigate these disadvantages, different semiconductor deposition techniques have been used, among the most used are immobilized films on different substrates (FTO, ITO, metal sheets and polymers), coating of lamps or surfaces of a reactor and different types of sponges and monoliths [9, 11–13]. However, the immobilization of the photocatalyst on substrates generally leads to a decrease in photocatalytic activity, reducing its efficiency by one tenth due to the low specific surface area and low dispersion of particles

and light absorption [10]. Therefore, the deposition of semiconductors on absorbent monolithic materials has aroused great interest, providing a stable matrix that improves oxidation-reduction processes, increasing recyclability [9–11]. A few years ago, our group reported the use of silica monolithic filters which showed excellent behavior for the adsorption and photodegradation of methylene blue dye (MB) under UV–visible light irradiation [14]. In fact, SiO_2 has been used as ceramic support for the deposition of ZnO, α-Fe_2O_3 metal oxides, which have energy bandgap values of 3.1 and 2.0 eV, respectively [15–17]. These catalysts are easily synthesized by soft chemistry methods, as well as being abundant and economically suitable, which suggests that they are appropriate for deposition on a monolithic filter. On the other hand, silica filters are materials used in different industries, due to its various physico-chemical properties, such as: high absorption capacity, being an excipient material, possessing pyroelectric and piezoelectric properties, and be the second most abundant material on the planet [18–19]. Also, it has been reported that SiO_2 template limits the agglomeration in the growth of nanoparticles, favors good dispersion and improves photonic absorption and charge transportation [20]. In addition, it favors the reduction of photoluminescence emission associated with the recombination of charge. Another application of silica is its use as an intermediate which improves the adsorption and stability of the compound due to the porous surface of the silica and the electron storage capacity of the semiconductor deposited on the surface with high oxidation capacity [21–22]. Therefore, this paper reports the preparation of ZnO-Fe_2O_3@SiO_2 monolithic filters exfoliated by hydrothermal method to promote the separation of photogenerated charges, as well as to improve the stability of this compound. In addition, these filters were evaluated in a CPC photocatalytic reactor, looking for better photocatalytic efficiency for the degradation of organic compounds such as methylene blue. Morphology, oxidation states of the metal oxides on the surface, adsorption capacity, oxidizing species identification and photocatalytic recyclability of the monolithic filters are discussed too in this paper.

2. EXPERIMENTAL

2.1 Materials and methods.

SiO_2 commercial ceramic supports (BIOMAX) and ammonia solution (99%, DEQ, CAS: 1336-21-6) were used to adjust the pH for all experiments. Exfoliation of monolithic filter was performed by hydrothermal method [14].

2.2 Synthesis of ZnO@SiO_2.

First, the monolithic filter was immersed in deionized water for 60 min to ensure maximum water absorption, then zinc acetate 0.489 M was added until completely dissolved. Immediately, NH_4OH was used to adjust pH to 8, after that, polyvinyl pyrrolidone (PVP) (0.3 g) was added. The resulting solution and the monolithic filter were transferred to a Teflon-lined and heated at 180°C for 14 h, for the exfoliation process and the *in-situ* crystallization of ZnO. The recovered solid was washed with water and ethanol to neutralize the solution and finally dried to 80°C for 6 h.

2.3 Synthesis of Fe_2O_3@SiO_2.

The monolithic filter was immersed in deionized water for 60 min. 0.696 M of ferric nitrate was added. Subsequently, KOH (5 M) was added up to increase pH to 12. The resulting solution and the monolithic filter were transferred to a Teflon-lined and heated at 120°C for 8 h.

2.4 Synthesis of ZnO-Fe_2O_3@SiO_2.

The preparation of monolithic filter ZnO-Fe_2O_3@SiO_2 was carried out in two steps. First, the deposition of the zinc oxide particles is carried out, as outlined in section 2.2. After that process, the iron oxide particles are deposited using the previously synthesized monolithic ZnO@SiO_2 filter, as detailed in previous section. Finally, the recovered monolithic filters were washed with distilled water and ethanol to neutralize the solution and finally dried at 80°C for 12 h.

2.5 Monolithic filters characterization.

All monolithic filters were analyzed by X-ray diffraction (XRD) using a PANalytical Empyrean diffractometer with CuKα radiation (λ = 1.5418 Å) at a scanning range of 10–70 degrees and scan rate of 0.02 degrees per minute to analyze the phase formation and crystalline structure. Morphology of materials was analyzed by scanning electron microscope (SEM) JEOL JSM6490 LV operated at 20 kV and equipped with microanalysis dispersion X-rays (EDS) for chemical quantification. The oxidation states of the metal oxides on the surface of monolithic filter were determined by X-ray photoelectron spectroscopy (XPS) using a Thermofisher XPS Escalab 250Xi equipped with an Al Kα (1486.68 eV) monochromatic radiation. The surface area was determined by N_2 adsorption measurement at 77 K using a Mini Belsorp II (Bel Japan). All the samples were vacuum dried at 300°C for 1 h before the test. Dye degradation was followed by measuring the absorbance value at 663 nm in a UV-vis NIR spectrophotometer (Cary 5000) in the range of 200–800 nm. To determine the degree of MB mineralization, total organic carbon (TOC) analysis was conducted in a Shimadzu 5000 model equipment. Kinetic of the reaction was monitored by HPLC liquid chromatography using a Shimadzu equipment model LC-2030C with a C18 5 µm column (50 X 3.0 mm) and a PDA detector (λ = 264 nm), with a mobile phase of methanol, water (70:30), with a retention time of 5 min, and a flow rate of 0.5 µm, excited at a wavelength of 246 nm, while for DXT, the mobile phase was acetonitrile and water (50:50), with a retention time of 1.12 min, and a flux of 10 µm, excited at a wavelength of 254 nm.

2.6 Photocatalytic degradation.

The experiments were carried out in a Pyrex glass reactor (150 ml), equipped with a propeller stirrer with a constant stirring rate of 150 rpm, illuminated with a xenon (Xe) lamp of 35 W (400–700 nm), 3200 lumens and 6000 K, maintaining a temperature around 30°C. The photocatalytic experiment was conducted with 100 ml of solution for each monolithic filter used. The solution was stirred in dark for 60 min before the light was switched on to ensure adsorption-desorption equilibrium. Aliquots of 3 ml were taken at a regular time interval and measured in the UV-Vis equipment and in the HPLC equipment.

The degradation rate was calculated by Eq. 1 [7]

$$d\,(\%) = \frac{A_0 - A_t}{A_0} X\ 100 \ldots \text{(Eq. 1)}$$

Where *d* is degradation rate, A_t is absorption after radiation and A_0 is absorption before radiation.

To determine the oxidizing species used in the degradation process of the organic molecule during the reaction, different chemical agents were added to trap the species generated during the process. The procedure to determine the oxidizing species (h^+, OH., H_2O_2 and O_2^-) was like the previously described for the photocatalytic evaluation. Table 1 showed the chemical reagents and the corresponding dye concentration.

Table 1
Chemical agents for determination of oxidizing species.

Chemical reagent	Species	Concentration (MB)
KI	h^+	0.0006 g
Isopropanol	OH·	0.003 ml
Catalase	H_2O_2	0.06 g
Benzoquinone	O_2^-	0.0004 g

On the other hand, recyclability tests were carried out to determine the average lifetime of the monolithic filters. To determine the surface pore saturation and adsorption capacity, filters were dried at 80°C for 12 h, without additional treatment. The monolithic filter is evaluated in three consecutive cycles, without any further treatment of washes, in the degradation of the methylene blue dye.

3. RESULTS AND DISCUSSION

3.1 X-ray diffraction (XRD).

Figure 1 shows the X-ray diffraction pattern of the monolithic filters with the incorporation of the metal oxide particles (ZnO and Fe_2O_3) deposited. It is observed that the XRD pattern of the monolithic silica filter (a) chemically treated by the hydrothermal method at 180ºC for 14 hours showed the presence of the phases identified as α-cristobalite, β-quartz, Na_2O and Al_4O_4C. During the exfoliation of the monolithic silica filter (b) it was observed that the increment in temperature during hydrothermal treatment and the pressure generated inside the reactor causes a variation in the length and angle in the silicon and oxygen bonds, favoring the crystallization of the α-cristobalite and the formation of silanoles Q^2 (Si-OH) and Q^3 (O_3-Si-OH) which have been related to the adsorption capacity and stability of SiO_2 [14].

On the other hand, the monolithic filter with zinc oxide particles ($ZnO@SiO_2$) (c) showed the presence of highly crystalline particles of the ZnO, evidenced by the existence of the three representative peaks of the material at 31.73, 34.37, and 36.21º (JCPDS 01-070-8070). Likewise, XRD pattern of $Fe_2O_3@SiO_2$ (d) showed low crystallinity of Fe_2O_3 (JCPDS 00-033-0664) peaks, which are overlapped by the SiO_2 peaks which normally present high crystallinity. Additionally, the diffractogram of the monolithic filter deposited with particles of zinc oxide and iron oxide ($ZnO\text{-}Fe_2O_3@SiO_2$) (e), showed mainly the presence of ZnO and SiO_2 peaks, while peaks of Fe_2O_3 particles are not detected due to its low crystallinity.

3.2 X-ray photoelectron spectroscopy analysis (XPS).

XPS analyses were performed to determine the oxidation states and elements present on the surface of the monolithic filters that were deposited with ZnO and Fe_2O_3 particles. Figure 2 shows the XPS spectrum of the exfoliated filter, comparing the $ZnO@SiO_2$, $Fe_2O_3@SiO_2$, and $ZnO\text{-}Fe_2O_3@SiO_2$ filters. In the filter spectrum $ZnO@SiO_2$, it is observed the signals from Zn $2p_3$ to 1021.16 eV and Zn $2p_1$ to 1043.90 eV, which demonstrate the existence of ZnO [23]. On the other hand, the filter $Fe_2O_3@SiO_2$ shows a spectrum similar to the exfoliated monolithic filter, with a slight emission of Fe 2p at 710.23 eV corresponding to the Fe^{3+} cation of hematite ($\alpha\text{-}Fe_2O_3$) [24]. Finally, the spectrum corresponding to the filter $ZnO\text{-}Fe_2O_3@SiO_2$ is shown, which stands out for exhibiting more intense Fe emissions in 710.98 and 724.53 eV, which correspond to Fe $2p_{3/2}$ and Fe $2p_{1/2}$, which agrees with the previously reported [24–25]. This result corroborates the presence of Fe_2O_3 on the surface of the monolithic filter.

Figure 2b shows the decovolution of the elements present on the surface of the $ZnO\text{-}Fe_2O_3@SiO_2$ monolith. Subsection (a) shows the spectra of Si 2p which shows three components of SiO_2 to 101.43 eV, Si-O-Si to 102.36 eV and Si-OH to 103.33 eV [26–27]. In section (b) O 1s peaks are shown, the high peak (O_L) at 531.85 eV corresponds to the O_2^- ions frequently surrounded by Si ions in the SiO_2 structure. The O_V peak at 531.03 eV is due to oxygen vacancies, and the O_C peak at 529.7 eV is related to chemisorbed oxygens species. In section (c) shows three peaks of the adjusted Fe 2p spectrum, peaks at 710.8 and 713.1 eV were indexed to Fe $2p_{1/2}$, and peak 724.8 eV corresponds to Fe $2p_{3/2}$. While peaks at 719.1 and 732.7 eV were assigned to the Fe^{3+} of the $\alpha\text{-}Fe_2O_3$ [25, 28]. On the other hand, subsection (d) shows the spectrum Zn 2p divided into two peaks at 1044 and 1021.22 eV corresponding to Zn $2p_{1/2}$ and Zn $2p_{3/2}$, respectively, which are assigned to the tetrahedral Zn with a 2 + oxidation state. Zn $2p_{3/2}$ peak could originate in Zn-O bonds, in addition, it could be considered a weak peak at 1022.73 eV attributed to Zn-OH because hydrogen has a greater electronegativity than Zn, which leads to a higher density of positive charge in the atoms attached to the OH groups [29–32].

3.3 Morphology of monolithic filters by scanning electron microscopy (SEM).

A surface analysis was performed using the SEM technique on the internal and external surface of the monolithic filter. Figure 3 corresponds to the SEM images of the monolithic filter exfoliated by the hydrothermal method and the filters deposited with the metallic oxides (ZnO and Fe_2O_3). Section a-b show a rough surface on the filters, which breaks into scales and falls off the surface, leading to the formation of small spherical particles of about 1 μm. Cracking and surface breakage is mostly influenced by reaction time, while the pH of the solution defines the particles cracked on the surface spherically, as reported by Xu Hai Yan et al., that the NH^{4+} ion can modify the growth of crystals under hydrothermal conditions [14, 33]. The surface modification of the silica filter caused by the hydrothermal process is due to a random rupture of the silicon-oxygen bonds. The different atomic arrangement and the various forms of bond break Si-O in the β-quartz and α-cristobalite crystalline structures gave rise to a different microstructure on the surface. Which could play a crucial role in adsorption processes and the deposition of semiconductors on the surface [34].

Section c-d shows the zinc oxide particles in the form of hexagonal prisms deposited on the monolithic filter. The internal surface shows a morphology of well-defined bars up to 5 μm in diameter that grow from a nucleus, and these are stretched to achieve the observed shape. While, on the outer surface, stands out the growth of ZnO bars on a rough surface, which were cultivated and grown on the surface of the silica filter and acts as a template for the continuous infiltration of Zn^{2+} on the exfoliated surface, and some particles of $Zn(OH)_2$ that continue to crystallize as a hexagonal prism separating from the silica base. This crystallization mechanism is like that reported by other authors [12, 35–36]. The morphological difference in zinc oxide particles on the external and internal surface of the filter is due to the absorption capacity of zinc ions on the surface of exfoliated silica during nucleation [37].

While, in the section e-f show the SEM images of the monolithic filter with particles of α-Fe_2O_3 deposited on the surface. The SiO_2 matrix limits the growth of α-Fe_2O_3 particles during the nucleation process. The particles deposited on the internal and external surface of the filter show a homogeneous size and less than 1 μm, with a morphology of leaves and needles [38–39].

On the other hand, in (g-h), the monolithic filter ZnO-Fe_2O_3@SiO_2 shows a completely cracked surface product of the hydrothermal process in the metal oxides deposit. In the paragraph (g) it is possible to perceive hexagonal prisms of ZnO on the surface, while in section (h) it shows a corrugated strip in the form of leaves, like that observed in (d) where the particles of ZnO are deposited and grow. Similar to that observed by Yanjun Liu et al., Fe^{3+} ions adhere and distribute on the silica surface, some others adsorb on the ZnO surface to form ions of $[Fe(OH)_4]^-$, during the hydrothermal process they lose OH^- and H_2O allowing the growth of α-Fe_2O_3 particles [40–41].

Deposition of metal oxides on the surface of the silica filter depends on the adsorption capacity [12]. SiO_2 matrix prevents agglomeration of deposited particles [41]. Those particles that fail in inserting into the silica surface or adhering to previously deposited zinc particles did not crystallize. Similarly, the inner and outer part of the monolithic filter shows different adsorption capacity, product of surface exfoliation

by hydrothermal method, which is important because surface exfoliation causes a greater pore generation and consequently a greater affinity for the growth of particles on the surface.

EDS point analysis and mapping of the ZnO-Fe_2O_3@SiO_2 filter were performed to determine the chemical composition and study the distribution of the elements present. Figure 4a shows two points on the surface of the monolithic filter. Spectrum 1 indicates the corrugated morphology in the form of leaves, the elements mostly present are the Si, Zn and O (showed in insert of spectrum 1). Demonstrating the growth of ZnO particles in this area, which corresponds to morphology results previously observed in Fig. 3d, and in a smaller percentage, the presence of Fe particles deposited and distributed over the same area can be detected also. Spectrum 2 indicates a smooth morphology on the filter surface, which corresponds to SiO_2 according to elemental analysis (showed in insert of spectrum 2). Similarly, a low percentage of Fe is detected, confirming that Fe_2O_3 is homogenously deposited and distributed on the silica surface and ZnO particles. The presence of each one of the elements detected by mapping is shown in Fig. 4b (Si), 4c (Zn) and 4d (Fe).

Table 2 shows the BET (Brunauer–Emmett–Teller) results for surface area diameter and average pore volume of monolithic filters. According to the results it can be mentioned that the silica monolithic filters have a low interaction between the adsorbent surface and the adsorbate, this is due to the high crystalline nature of the materials as observed by XRD, obtaining a surface area with values between 2–3 m^2/g. After the hydrothermal exfoliation process, the silica filter slightly increases the surface area and pore volume with respect to the raw filter.

The Fe_2O_3 particle deposit does not represent an apparent change from the exfoliated filter, on the other hand, ZnO particle deposited shows an increase in the surface area and pore volume [9, 42]. However, these results are not determinant because there is no significant difference between each sample and may not be related to the photocatalytic properties of the monolithic filter.

Table 2
Surface area, volume, and pore diameter of monolithic filters.

Sample	Surface area (m^2/g)	Pore volume (cm^3/g)	Pore size (nm)
Raw Filter	0.32	0.0742	106.52
Exfoliated filter	1.57	0.3621	24.74
ZnO@SiO_2	2.56	0.5897	24.30
Fe_2O_3@SiO_2	1.58	0.3638	31.74
ZnO-Fe_2O_3@SiO_2	2.34	0.5378	24.06

3.4 UV–visible diffuse reflectance spectroscopy.

Figure 5a shows the UV-Vis spectra to study the optical properties of monolithic silica filters synthesized with ZnO and Fe_2O_3 particles. While in Fig. 5b the energy band structure diagram of ZnO-Fe_2O_3@SiO_2 is showed. The bandgap energy of the samples was calculated using the Kubelka-Munk function. Raw and exfoliated filters show an intrinsic absorption in the ultraviolet region leading bandgap values of 3.7 and 3.8 eV, respectively. However, when ZnO was incorporated on the filters (ZnO@SiO_2), the E_g value increases until 4.5 eV. While addition of Fe_2O_3 provoked a considerable diminishing of the E_g value on the filters (Fe_2O_3@SiO_2), which is around of 1.9 eV. This demonstrates that the presence of metal oxide on the filter surface has influence on the absorption in the UV-Visible spectrum. On the other hand, the ZnO-Fe_2O_3@SiO_2 heterojunction presented a bandgap value of 3.3 eV, which it can absorb more photons and generate a greater number of electrons and holes, which could be favoring a better photocatalytic activity under ultraviolet and visible region.

3.5 Methylene blue (MB) degradation by photocatalysis.

The photocatalytic efficiency of the filters was evaluated in the degradation of MB dye at 10 ppm. Figure 6a shows that the deposition of metal oxides has a direct influence on the surface adsorption capacity of the molecule, and subsequently on the degradation of the dye. In this case, activity of raw filter was improved 43 and 57% when ZnO and α-Fe_2O_3 were deposited, respectively. This result was due to the adsorption capacity of the ZnO@SiO_2 and Fe_2O_3@SiO_2 filters, which is correlated with the bandgap and the particle size of the metal oxides deposited on the filter surface. Particularly, it is reported that nanometric particle size of α-Fe_2O_3 allows greater generation of active sites to adhere the organic molecule and then react with the semiconductor [43]. Therefore, filters containing Fe_2O_3 particles showed better absorption which enhances discoloration of the dye. According to the observed in Fig. 6a, ZnO-Fe_2O_3@SiO_2 filter shows an adsorption capacity superior to the raw filter and ZnO@SiO_2, and slightly lower than exfoliated filter and Fe_2O_3@SiO_2. From the above results, it is concluded that deposition of semiconductors on the filter surface causes a loss in porosity and adsorption of the dye. However, the presence of metal oxides (ZnO and α-Fe_2O_3) improves oxide-reduction throughout the reaction process, maintaining a constant kinetics and high degradation efficiency (94%) for ZnO-Fe_2O_3@SiO_2.

The changes in the UV-Vis absorption spectrum of MB during photocatalytic degradation corroborated the effect of using the ZnO-Fe_2O_3@SiO_2 filter as catalyst, Fig. 6b. Specifically, the intensity of the spectrum when this semiconductor is used decreased steadily after the adsorption process. In addition, a peak at smaller wavelengths, between 200 and 250 nm, is observed, which is attributed to the generation of oxidative radicals and the insertion of OH into the organic molecule, which leads to a bathochromic effect at the peak of maximum absorbance at 663 nm.

On the other hand, Fig. 6c shows the reaction kinetics of monolithic filters, which demonstrated that ZnO-Fe_2O_3@SiO_2 filter shows a linear behavior with the highest reaction speed and lowest half-time life

(25 times lower than raw filter), which indicates an exponential decay with values close to a first order reaction.

In addition, recyclability tests were carried out on the ZnO-Fe_2O_3@SiO_2 filter where it can be observed that after three reaction cycles the efficiency keeps intact (94 ± 1% after each cycle), Fig. 6d. This result indicates that the combination of ZnO and Fe_2O_3 deposited on surface filters to obtain ZnO-Fe_2O_3@SiO_2 monolithic filters are a viable option that improve recyclability processes and keeps degradation efficiency, which could facilitate practical applications in scaling photocatalytic processes.

Table 2 shows the percentage of degradation, and the half-time life of each monolithic filter evaluated during three consecutive cycles in MB degradation. The results indicate that the ZnO-Fe_2O_3@SiO_2 filter keeps the degradation percentage intact after three reaction cycles (94, 95, 94%, during first, second and third cycle, respectively). While efficiency of the exfoliated filter, Fe_2O_3@SiO_2 and ZnO@SiO_2 decreased its effectiveness 34, 30 and 13%, from the first, second and third cycle, respectively. Similarly, the ZnO-Fe_2O_3@SiO_2 filter maintains a lower half-time life in all reaction cycles, showing a reaction rate of k = 0.0075 and R^2 = 0.997, markedly higher than the other synthesized filters.

Table 2
Percentage of MB degradation, reaction kinetics, half-time life ($t_{1/2}$) over 3 reaction cycles.

Sample	**Degradation cycle 1–3**			**$t_{1/2}$ (min) cycle 1–3**			**Reaction kinetics first cycle**	
	%D-1	**%D-2**	**%D-3**	**C-1**	**C-2**	**C-3**	**R^2**	***k***
Raw filter	37	35	24	2310	2657	2763	0.893	0.0003
Exfoliated filter	94	70	60	105	330	385	0.959	0.0066
ZnO@SiO_2	79	70	66	165	231	239	0.973	0.0042
Fe_2O_3@SiO_2	96	94	66	224	150	239	0.701	0.0026
ZnO-Fe_2O_3@SiO_2	95	96	94	92	77	112	0.997	0.0075

TOC analysis of the reaction product was performed at 300 min reaction using the different monolithic filters to determine the percentage of mineralization of the molecule. Figure 7a shows the TOC percentage during each reaction cycle, where it is observed that the ZnO-Fe_2O_3@SiO_2 filter was able to mineralize 66% of the MB dye during the first cycle and decreased only 10% after subsequently cycles. The efficiency of the ZnO-Fe_2O_3@SiO_2 filter increased the mineralization percentage by 48 and 51% compared to the α-Fe_2O_3@SiO_2 and ZnO@SiO_2 filters, respectively. These results demonstrate that the adsorption and degradation process of the exfoliated filter is high, but stability is only reached by depositing of the metal oxides ZnO and α-Fe_2O_3, enhancing the mineralization process too. In

conclusion, the monolithic silica filter is an excellent material that acts as a support for the deposition of semiconductors to obtain effective materials for photocatalytic degradation.

To understand the reaction mechanism, the reactive species responsible for the photocatalytic degradation process were identified using several scavengers. Figure 7b shows the addition of potassium iodide as a hole scavenger (h^+), isopropanol for the capture of hydroxyl radicals (•OH), catalase as a scavenger of peroxide radicals (H_2O_2) and benzoquinone as a scavenger of superoxide radicals (O_2^-). It was determined that peroxide and hydroxyl radicals are those that have a greater interference to control the degradation reaction of the MB dye. While the holes and superoxide radicals influence photocatalytic activity to a lesser extent.

3.6 Infrared spectroscopy (IR).

Additionally, a liquid-liquid extraction was performed on the reaction product of the degradation reaction of MB after the first cycle to follow up the molecule breakage using the FTIR technique. Figure 8a shows the reaction product of the exfoliated filter, and the Fe_2O_3@SiO_2, ZnO@SiO_2 and ZnO-Fe_2O_3@SiO_2 filters. It is observed that the reflections corresponding to alkane groups (CH) at 2971 cm^{-1}, secondary amines (CH-NH-CH) at 1463 cm^{-1}, aliphatic aldehydes (CH_2-CHO) at 1369 cm^{-1} and aliphatic ethers (CH_2-O-CH_2) at 954 cm^{-1} are the only reflections remaining after 300 min of reaction. The IR spectra of ZnO-Fe_2O_3@SiO_2 filter showed that bonds present low intensity reflections, indicating absence of the dye molecule after the degradation process, corroborating the efficiency of the monolithic ZnO-Fe_2O_3@SiO_2 silica filter for the degradation of MB dye, as it was observed in the UV-Vis, and TOC analyses.

According to the above results it was possible to propose a mechanism of the breakage of the methylene blue dye molecule using the ZnO-Fe_2O_3@SiO_2 filter, which is showed in Fig. 8b. It is assumed that the dye bond breaking starts in the central part of the molecule, destroying the double bond of the benzene ring. This assumption is supported by the bathochromic effect observed by UV-Vis. Thus, it causes a loss of color during the first minutes of reaction. The high generation of oxidizing species provoked by the presence of the deposited ZnO and α-Fe_2O_3 semiconductors, causes the breaking of the bonds of the dye until mineralization, it means to convert the molecule to CO_2 and H_2O [44–46].

CONCLUSIONS

Deposition of ZnO and α-Fe_2O_3 particles on monolithic silica filters was successfully achieved by hydrothermal method and the presence of these deposited elements was verified by EDS analysis. XRD, SEM-EDS and XPS analysis corroborates the presence of all phases, ZnO, SiO_2 and Fe_2O_3, exhibiting that ZnO and Fe_2O_3 particles are deposited onto silica filters. ZnO-Fe_2O_3@SiO_2 filters showed to be highly effective when used in the CPC photocatalytic reactor because enhance the reaction stability in the degradation of methylene blue (MB) dye, with 95% efficiency remaining intact after three reaction cycles. In addition, the deposited semiconductors improved the reaction kinetics by mineralizing 66% of the dye

in the first cycle and decreasing to 10% for the third reaction cycle. The presence of metal oxides (ZnO and α-Fe_2O_3) promotes oxidation-reduction reaction during the degradation process, maintaining high reproducibility of degradation using MB after 3 cycles. In addition, the proposal mechanism indicates that the high generation of oxidizing species (peroxide and hydroxyl radicals), provoked by the presence of the deposited ZnO and α-Fe_2O_3 semiconductors, causes the breaking of the bonds of the dye until mineralization. Therefore, ZnO-Fe_2O_3@SiO_2 monolithic filters prepared in this work are excellent materials that acts as a support for the deposition of semiconductor materials to obtain effective materials for photocatalytic degradation, which could be as an innovative alternative for water treatment, due to its easy preparation, practicality and recyclability, for its use in a CPC photocatalytic reactor.

Declarations

Author Contribution

"I. Juárez-Ramírez. Intellectual contribution; draft of the paper; experimental design; interpretation of data; discussion of the results; responsible of project with financial support; revision and approval of the manuscript""A. S. Galindo-Luna. Intellectual contribution; draft of the paper; experimental design; collection, analysis and interpretation of data; discussion of the results; revision and approval of the manuscript""M. E. Zarazúa-Morín. Intellectual contribution; draft of the paper; experimental design; discussion of the results; revision and approval of the manuscript""D. Sánchez-Martínez. Draft of the paper; discussion of the results; revision and approval of the manuscript""V. J. Gallegos-Sánchez. Draft of the paper; discussion of the results; revision and approval of the manuscript"

Acknowledgement

Authors would like to thank SECIHTI. A. Sebastián Galindo-Luna thanks to SECIHTI for scholarship No. 783128. Thank you to UANL for the financial support through PROACTI 2024 (113-IDT-2024). We also thank the staff of Ecomateriales and Energy Department and Materials Construction Laboratory at Civil Engineering Institute of the Civil Engineering Faculty at UANL. In addition, thanks to Dr. Francisco Servando Aguirre Tostado from CIMAV-Mty for his support with the XPS analysis.

References

1. Miriam Janet Gil, Adriana María Soto, Jorge Iván Usma, O. D. G. (2012). Contaminantes emergentes en aguas, efectos y posibles tratamientos. *Producción + Limpia*, *7*, 52–73.
2. Becerril, J. (2009). Contaminantes emergentes en el agua. *Revista Digital Universitaria*, *10*(8), 1–7. http://www.revista.unam.mx/vol.10/num8/art54/int54.htm
3. Thomas, E., Mendonça, F., Xavier, T. P., Souza, D. R. De, De, J. A., Eduardo, A., Jung, C., Oliveira, L. De, Zentrum, D., Höhe, L., & Porz, D.-K. (2005). Construção e estudos de perfomance de um reator fotoquímico tipo cpc (“compound parabolic concentrator”). *Quimica Nova*, *28*(5), 921–926.

4. Sánchez-Orozco, R., Martínez-Juan, M., García-Sánchez, J. J., & Ureña-Núñez, F. (2018). Removal of methylene blue from aqueous solution using Typha stems and leaves. *BioResources*, *13*(1), 1696–1710. https://doi.org/10.15376/biores.13.1.1696-1710
5. Papamija, M., & Sarria, V. (2010). Photocatalytic Degradation of Ibuprofen Using Titanium Dioxide. *Revista de Ingeniería*, *31*, 47–53.
6. Jing, D., Guo, L., Zhao, L., Zhang, X., Liu, H., Li, M., Shen, S., Liu, G., Hu, X., Zhang, X., Zhang, K., Ma, L., & Guo, P. (2010). Efficient solar hydrogen production by photocatalytic water splitting: From fundamental study to pilot demonstration. *International Journal of Hydrogen Energy*, *35*(13), 7087–7097. https://doi.org/10.1016/j.ijhydene.2010.01.030
7. Nguyen, C. C., Vu, N. N., & Do, T. O. (2015). Recent advances in the development of sunlight-driven hollow structure photocatalysts and their applications. *Journal of Materials Chemistry A*, *3*(36), 18345–18359. https://doi.org/10.1039/c5ta04326c
8. Liang, Q., Li, Z., Yu, X., Huang, Z. H., Kang, F., & Yang, Q. H. (2015). Macroscopic 3D Porous Graphitic Carbon Nitride Monolith for Enhanced Photocatalytic Hydrogen Evolution. *Advanced Materials*, *27*(31), 4634–4639. https://doi.org/10.1002/adma.201502057
9. Sharma, S., & Basu, S. (2020). Highly reusable visible light active hierarchical porous WO_3/SiO_2 monolith in centimeter length scale for enhanced photocatalytic degradation of toxic pollutants. *Separation and Purification Technology*, *231*(June 2019), 115916. https://doi.org/10.1016/j.seppur.2019.115916
10. Lekshmi Mohan, V., Shiva Nagendra, S. M., & Maiya, M. P. (2019). Photocatalytic degradation of gaseous toluene using self-assembled air filter based on chitosan/activated carbon/TiO_2. *Journal of Environmental Chemical Engineering*, *7*(6), 103455. https://doi.org/10.1016/j.jece.2019.103455
11. Silas, K., Ghani, W. A. W. A. K., Choong, T. S. Y., & Rashid, U. (2018). Breakthrough studies of Co3O4 supported activated carbon monolith for simultaneous SO_2/NO_x removal from flue gas. *Fuel Processing Technology*, *180*(May), 155–165. https://doi.org/10.1016/j.fuproc.2018.08.018
12. Wang, W., An, T., Li, G., Li, Y., Yu, J. C., & Wong, P. K. (2018). Free-standing red phosphorous/silver sponge monolith as an efficient and easily recyclable macroscale photocatalyst for organic pollutant degradation under visible light irradiation. *Journal of Colloid and Interface Science*, *518*, 130–139. https://doi.org/10.1016/j.jcis.2018.02.008
13. Films, T., Morales-mejía, J. C., Almanza, R., & Gutiérrez, F. (2014). *Solar* Photocatalytic Oxidation of Hydroxy Phenols in a CPC Reactor with Thick ScienceDirect Solar photocatalytic oxidation of hydroxy phenols in a CPC reactor with thick TiO_2 films. *Energy Procedia*, vol. 57, pages 597-606. https://doi.org/10.1016/j.egypro.2014.10.214
14. Zarazúa-Morín, M. E., Galindo-Luna, A. S., Gallegos-Sánchez, V. J., & Juárez-Ramírez, I. (2022). Chemical exfoliation of silica filters used on methylene blue degradation by photocatalysis. *Chemical Papers*, *0123456789*. https://doi.org/10.1007/s11696-022-02253-6
15. Alvi, M. A., Al-Ghamdi, A. A., & ShaheerAkhtar, M. (2017). Synthesis of ZnO nanostructures via low temperature solution process for photocatalytic degradation of rhodamine B dye. *Materials Letters*,

204, 12–15. https://doi.org/10.1016/j.matlet.2017.06.005

16. Zhang, Y., Gu, J., Murugananthan, M., & Zhang, Y. (2015). Development of novel α-Fe_2O_3/$NiTiO_3$ heterojunction nanofibers material with enhanced visible-light photocatalytic performance. *Journal of Alloys and Compounds*, *630*, 110–116. https://doi.org/10.1016/j.jallcom.2014.12.193
17. Sun, T. W., Zhu, Y. J., Qi, C., Ding, G. J., Chen, F., & Wu, J. (2016). α-Fe_2O_3 nanosheet-assembled hierarchical hollow mesoporous microspheres: Microwave-assisted solvothermal synthesis and application in photocatalysis. *Journal of Colloid and Interface Science*, *463*, 107–117. https://doi.org/10.1016/j.jcis.2015.10.038
18. Munasir, Triwikantoro, Zainuri, M., & Darminto. (2015). Synthesis of SiO_2 nanopowders containing quartz and cristobalite phases from silica sands. *Materials Science- Poland*, *33*(1), 47–55. https://doi.org/10.1515/msp-2015-0008
19. Kim, D., Jin, Y. H., Jeon, K. W., Kim, S., Kim, S. J., Han, O. H., Seo, D. K., & Park, J. C. (2015). Blue-silica by Eu^{2+}-activator occupied in interstitial sites. *RSC Advances*, *5*(91), 74790–74801. https://doi.org/10.1039/c5ra15641f
20. Fuentes, K. M., Betancourt, P., Marrero, S., & García, S. (2016). Photocatalytic degradation of phenol using doped titania supported on photonic SiO_2 spheres. *Reaction Kinetics, Mechanisms and Catalysis*, *120*(1), 403–415. https://doi.org/10.1007/s11144-016-1097-3
21. Phanichphant, S., Nakaruk, A., & Channei, D. (2016). Photocatalytic activity of the binary composite CeO_2/SiO_2 for degradation of dye. *Applied Surface Science*, *387*, 214–220. https://doi.org/10.1016/j.apsusc.2016.06.072
22. Teixeira, S., Mora, H., Blasse, L. M., Martins, P. M., Carabineiro, S. A. C., Lanceros-Méndez, S., Kühn, K., & Cuniberti, G. (2017). Photocatalytic degradation of recalcitrant micropollutants by reusable Fe_3O_4/SiO_2/TiO_2 particles. *Journal of Photochemistry and Photobiology A: Chemistry*, *345*, 27–35. https://doi.org/10.1016/j.jphotochem.2017.05.024
23. Al-Gaashani, R., Radiman, S., Daud, A. R., Tabet, N., & Al-Douri, Y. (2013). XPS and optical studies of different morphologies of ZnO nanostructures prepared by microwave methods. *Ceramics International*, *39*(3), 2283–2292. https://doi.org/10.1016/j.ceramint.2012.08.075
24. Bagus, P. S., Nelin, C. J., Brundle, C. R., Lahiri, N., Ilton, E. S., & Rosso, K. M. (2020). Analysis of the Fe 2p XPS for hematite α Fe_2O_3: Consequences of covalent bonding and orbital splittings on multiplet splittings. *Journal of Chemical Physics*, *152*(1). https://doi.org/10.1063/1.5135595
25. Han, T., Wei, Y., Jin, X., Jiu, H., Zhang, L., Sun, Y., Tian, J., Shang, R., Hang, D., & Zhao, R. (2019). Hydrothermal self-assembly of α-Fe_2O_3 nanorings@graphene aerogel composites for enhanced Li storage performance. *Journal of Materials Science*, *54*(9), 7119–7130. https://doi.org/10.1007/s10853-019-03371-5
26. Kaur, A., Chahal, P., & Hogan, T. (2016). Selective fabrication of SiC/Si diodes by excimer laser under ambient conditions. *IEEE Electron Device Letters*, *37*(2), 142–145. https://doi.org/10.1109/LED.2015.2508479

27. Bywalez, R., Karacuban, H., Nienhaus, H., Schulz, C., & Wiggers, H. (2012). Stabilization of mid-sized silicon nanoparticles by functionalization with acrylic acid. *Nanoscale Research Letters*, *7*(1), 76. https://doi.org/10.1186/1556-276X-7-76
28. Hao, S., Wang, H., Yang, R. et al. (2021). Corn-like mesoporous SnO_2 /α-Fe_2O_3 heterostructure for superior TEA sensing performance. *Applied Physics A*, *252*, 127:252. https://doi.org/10.1007/s00339-021-04350-x
29. Qian, K. J., Chen, S., Zhu, B., Chen, L., Ding, S. J., Lu, H. L., Sun, Q. Q., Zhang, D. W., & Chen, Z. (2012). Atomic layer deposition of ZnO on thermal SiO_2 and Si surfaces using N_2-diluted diethylzinc and H_2O_2 precursors. *Applied Surface Science*, *258*(10), 4657–4666. https://doi.org/10.1016/j.apsusc.2012.01.054
30. Zhenzhen Li, H. C. and W. L. (2018). Full-Spectrum Photocatalytic Activity of ZnO/CuO/$ZnFe_2O_4$ Nanocomposite as a PhotoFenton-Like Catalyst. *Catalysts*, *8*, 557. https://doi.org/10.3390/catal8110557
31. Zhao, J., Ge, S., Pan, D., Pan, Y., Murugadoss, V., Li, R., Xie, W., Lu, Y., Wu, T., Wujcik, E. K., Shao, Q., Mai, X., & Guo, Z. (2019). Microwave Hydrothermal Synthesis of In_2O_3-ZnO Nanocomposites and Their Enhanced Photoelectrochemical Properties. *Journal of The Electrochemical Society*, *166*(5), H3074–H3083. https://doi.org/10.1149/2.0071905jes
32. Kim, H. J., Tak, Y. J., Park, S. P., Na, J. W., Kim, Y. G., Hong, S., Kim, P. H., Kim, G. T., Kim, B. K., & Kim, H. J. (2017). The self-activated radical doping effects on the catalyzed surface of amorphous metal oxide films. *Scientific Reports*, *7*(1), 1–10. https://doi.org/10.1038/s41598-017-12818-1
33. Xu, H. Y., Wang, H., Zhang, Y. C., He, W. L., Zhu, M. K., Wang, B., & Yan, H. (2004). Hydrothermal synthesis of zinc oxide powders with controllable morphology. *Ceramics International*, *30*(1), 93–97. https://doi.org/10.1016/S0272-8842(03)00069-5
34. Tang, C., Zhu, J., Li, Z., Zhu, R., Zhou, Q., Wei, J., He, H., & Tao, Q. (2015). Surface chemistry and reactivity of SiO_2 polymorphs: A comparative study on α-quartz and α-cristobalite. *Applied Surface Science*, *355*, 1161–1167. https://doi.org/10.1016/j.apsusc.2015.07.214
35. Aquino, P., Osorio, A. M., Ninán, E., & Torres, F. (2018). Caracterización de nanoparticulas de ZnO sintetizadas por el método de precipitación y su evaluación en la incorporación en pinturas esmalte. *Revista de La Sociedad Química Del Perú*, *84*(1), 5–17. https://doi.org/10.37761/rsqp.v84i1.151
36. Lops, C., Ancona, A., Di Cesare, K., Dumontel, B., Garino, N., Canavese, G., Hernández, S., & Cauda, V. (2019). Sonophotocatalytic degradation mechanisms of Rhodamine B dye via radicals generation by micro- and nano-particles of ZnO. *Applied Catalysis B: Environmental*, *243*, 629–640. https://doi.org/10.1016/j.apcatb.2018.10.078
37. Kumar, S. G., & Rao, K. S. R. K. (2015). Zinc oxide based photocatalysis: Tailoring surface-bulk structure and related interfacial charge carrier dynamics for better environmental applications. *RSC Advances*, *5*(5), 3306–3351. https://doi.org/10.1039/c4ra13299h

38. Kan, J., & Wang, Y. (2013). Large and fast reversible Li-ion storages in Fe_2O_3-graphene sheet-on-sheet sandwich-like nanocomposites. *Scientific Reports*, *3*, 1–10. https://doi.org/10.1038/srep03502
39. Liu, R., Jiang, Y., Lu, Q., Du, W., & Gao, F. (2013). Al_3 controlled synthesis and magnetic property of α-Fe_2O_3 nanoplates. *CrystEngComm*, *15*(3), 443–446. https://doi.org/10.1039/c2ce26111a
40. Liu, Y., Sun, L., Wu, J., Fang, T., Cai, R., & Wei, A. (2015). Preparation and photocatalytic activity of ZnO/Fe_2O_3 nanotube composites. *Materials Science and Engineering B: Solid-State Materials for Advanced Technology*, *194*, 9–13. https://doi.org/10.1016/j.mseb.2014.12.021
41. Ali, M., Tehseen, U., Ali, M., Ali, L., & Mumtaz, M. (2018). Study of uncoated and silica-coated hematite (α-Fe_2O_3) nanoparticles. In *Surfaces and Interfaces* (Vol. 13, pp. 196–204). https://doi.org/10.1016/j.surfin.2018.09.011
42. Sharma, M., Singh, J., & Basu, S. (2019). Efficient metal ion adsorption and photodegradation of Rhodamine-B by hierarchical porous Fe-Ni@SiO_2 monolith. *Microchemical Journal*, *145*(November 2018), 708–717. https://doi.org/10.1016/j.microc.2018.11.042
43. Nguyen-Phan, T. D., Huy, C. N., Kim, C. K., & Shin, E. W. (2015). Facile microwave-assisted synthesis and controllable architecture of three-dimensional nickel titanate. *CrystEngComm*, *17*(24), 4562–4574. https://doi.org/10.1039/c5ce00154d
44. Mondal, S., De Anda Reyes, M. E., & Pal, U. (2017). Plasmon induced enhanced photocatalytic activity of gold loaded hydroxyapatite nanoparticles for methylene blue degradation under visible light. *RSC Advances*, *7*(14), 8633–8645. https://doi.org/10.1039/C6RA28640B
45. Mohammad, T., & Morrison, H. (2000). Simultaneous Photoconjugation of Methylene Blue and cis-$Rh(phen)_2Cl_2^+$ to DNA via a Synergistic Effect. In *Photochemistry and Photobiology* (Vol. 71, Issue 4, p. 369). https://doi.org/10.1562/0031-8655(2000)071<0369:spomba>2.0.co;2
46. Yu, Z., & Chuang, S. S. C. (2007). Probing methylene blue photocatalytic degradation by adsorbed ethanol with in situ IR. *Journal of Physical Chemistry C*, *111*(37), 13813–13820. https://doi.org/10.1021/jp0715474

Figures

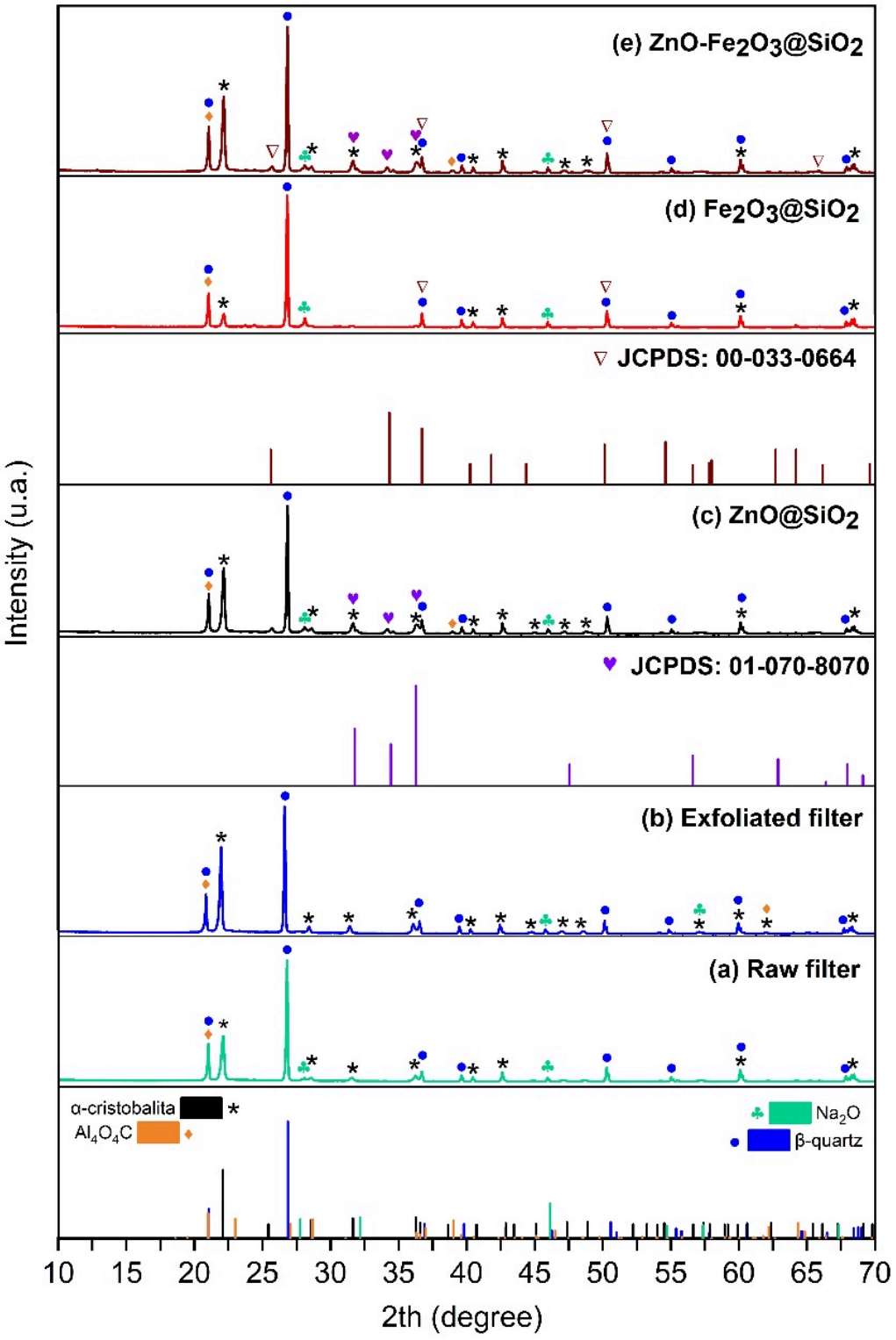


Figure 1

X-ray diffraction pattern of a) exfoliated monolithic silica filter, b) $ZnO@SiO_2$, y c) $ZnO\text{-}Fe_2O_3@SiO_2$.

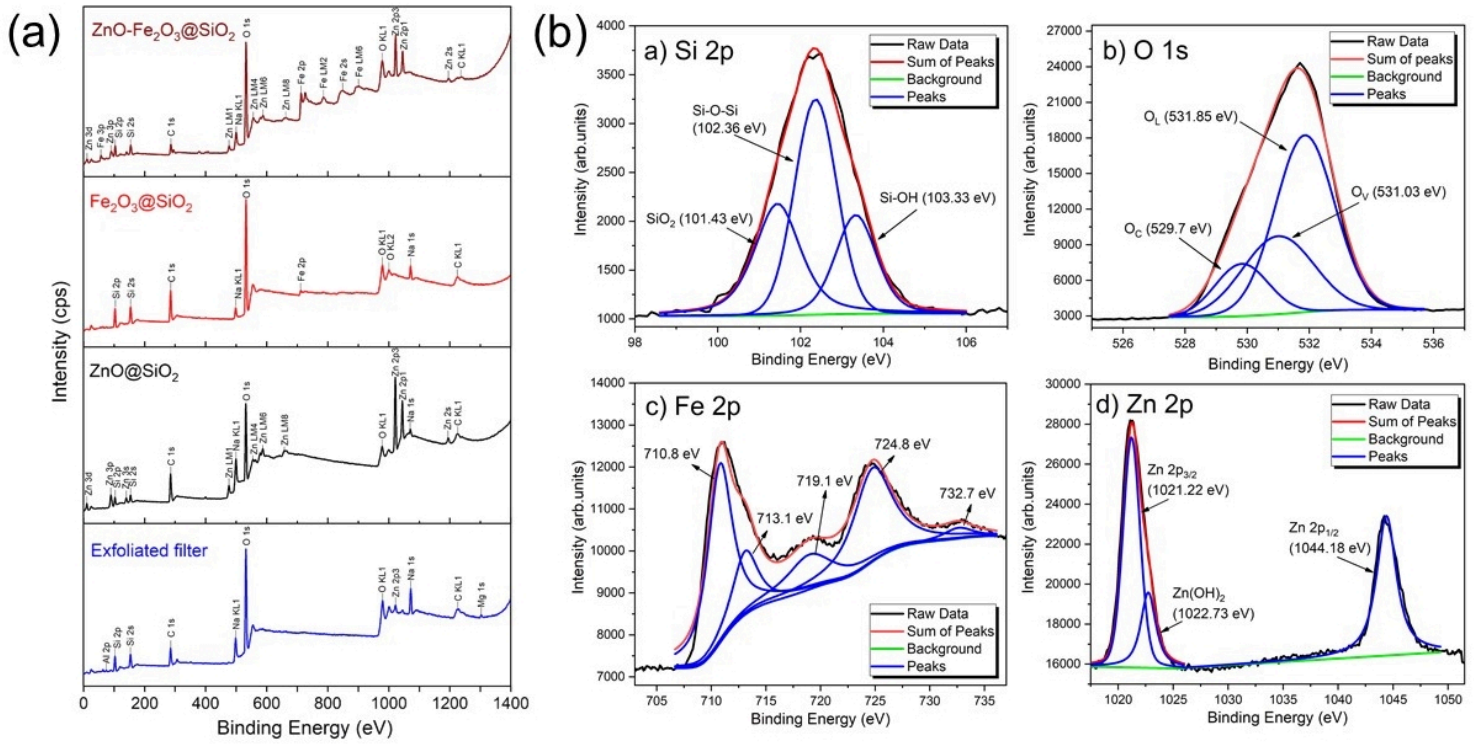


Figure 2

a) XPS survey Spectrum of filter exfoliated ZnO@SiO_2; Fe_2O_3@SiO_2 and ZnO-Fe_2O_3@SiO_2, b) XPS spectra deconvoluted a) Si 2p, b) O 1s, c) Fe 2p and d) Zn 2p of the monolithic filter ZnO-Fe_2O_3@SiO_2.

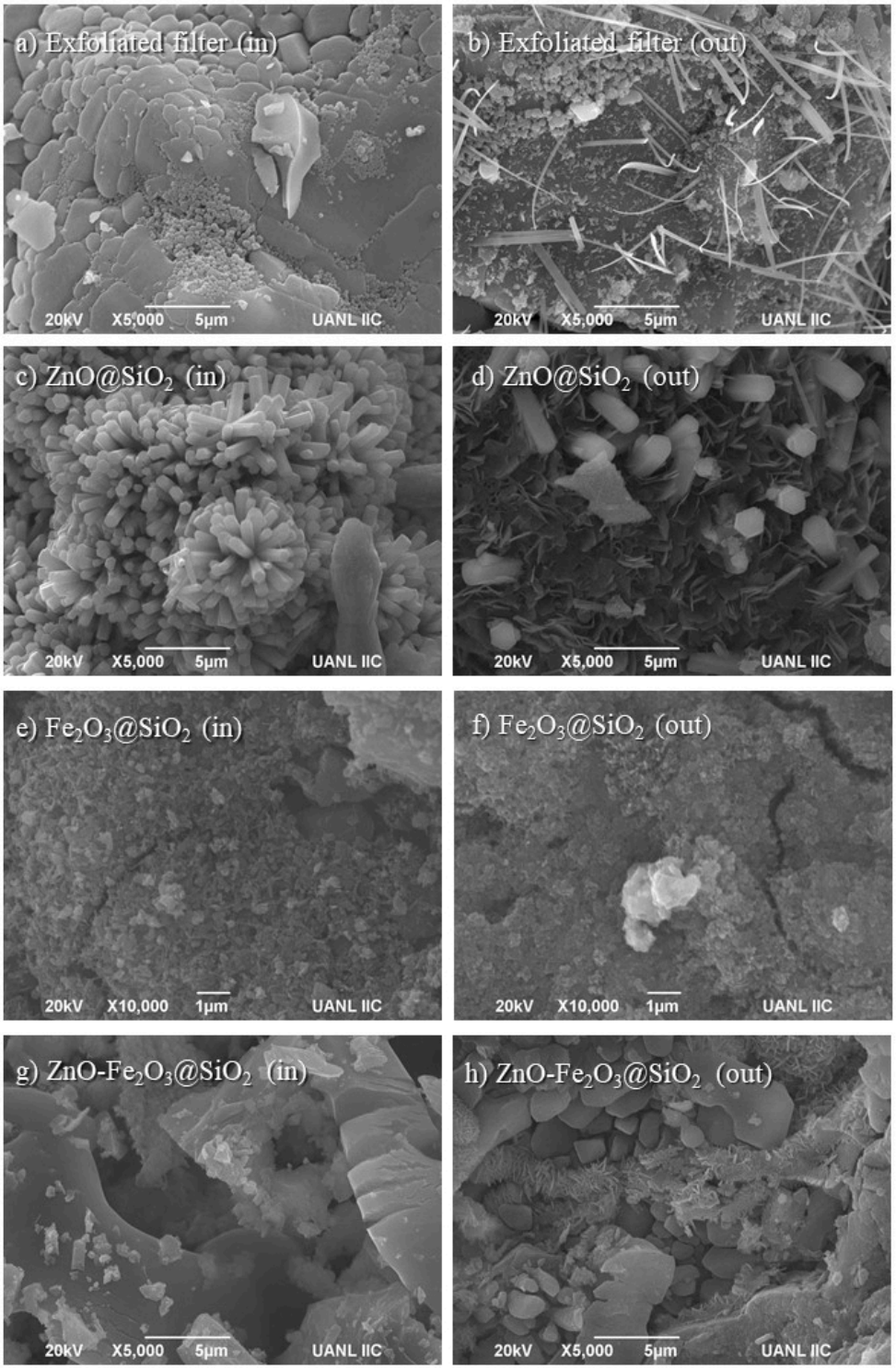
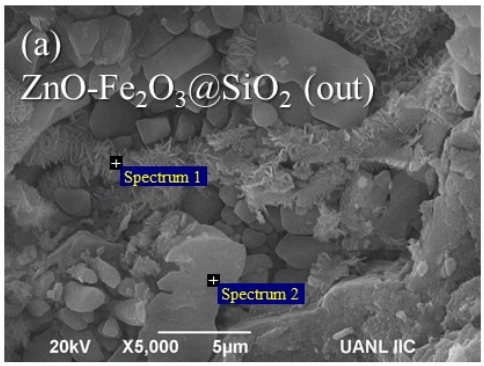


Figure 3

SEM images of the filters (a, b) exfoliated SiO_2; (c, d) $ZnO@SiO_2$; (e, f) $Fe_2O_3@SiO_2$; (g, h) $ZnO\text{-}Fe_2O_3@SiO_2$.



Spectrum 1		
Element	Weight%	Atomic%
C K	8.63	17.15
O K	29.17	43.52
Al K	4.58	4.06
Si K	27.80	23.62
K K	2.28	1.39
Fe K	3.45	1.47
Zn K	24.10	8.80

Spectrum 2		
Element	Weight%	Atomic%
C K	0.50	0.89
O K	43.55	57.76
Na K	2.15	1.99
Si K	50.08	37.84
K K	0.74	0.40
Fe K	2.98	1.13

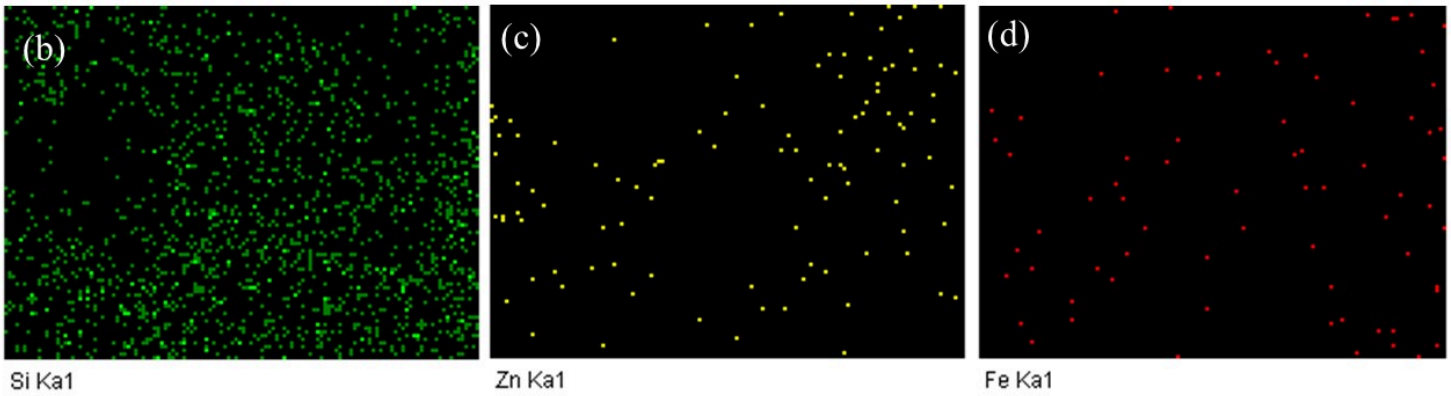


Figure 4

(a) EDS spectra with SEM micrograph of ZnO-Fe_2O_3@SiO_2, (b–d) elemental mapping.

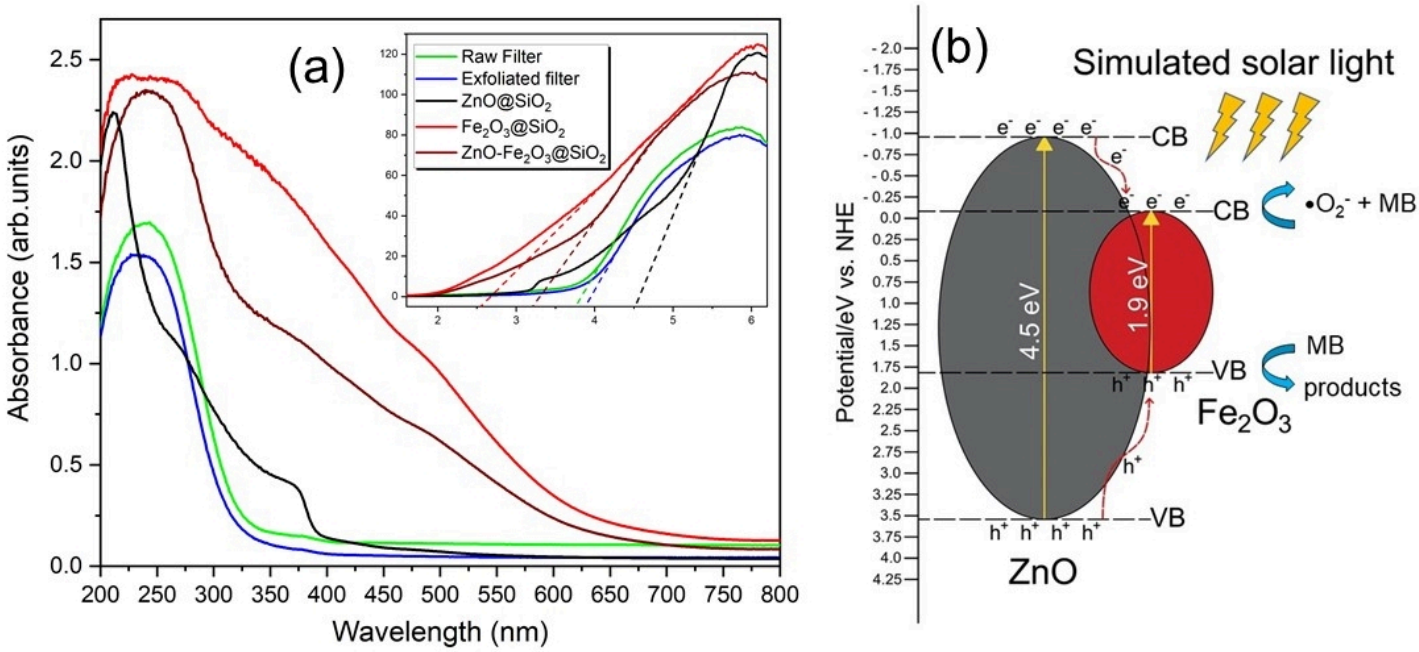


Figure 5

(a) Ultraviolet-visible absorption spectra of monolithic filters, (b) Energy band structure diagram of ZnO-Fe_2O_3@SiO_2.

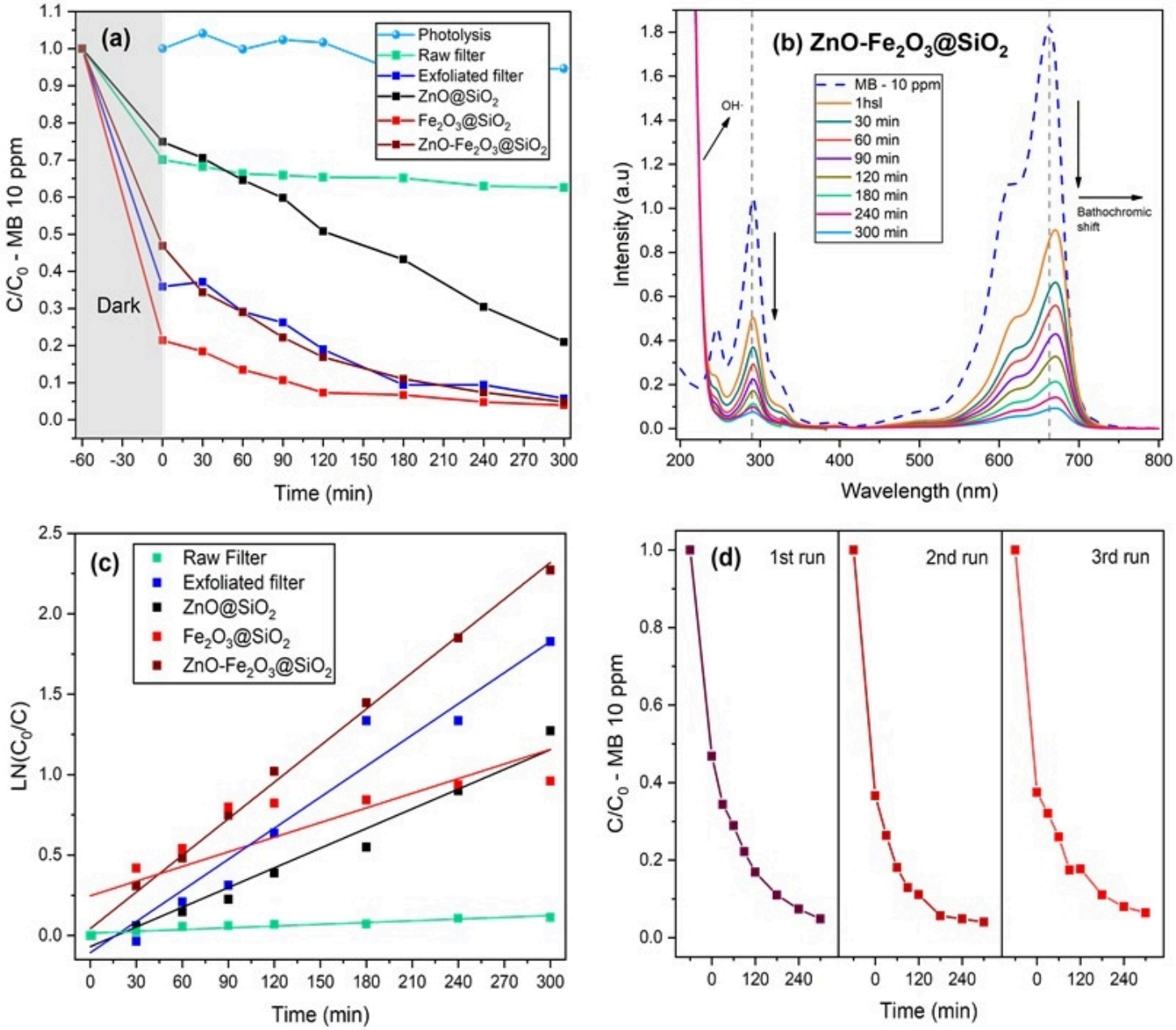


Figure 6

a) Photocatalytic degradation of MB; b) UV-Vis absorption spectra of MB using ZnO-Fe_2O_3@SiO_2 filter; c) Pseudo-first-order model linear fitting of synthesized monolithic filters; d) Photodegradation efficiency of MB over ZnO-Fe_2O_3@SiO_2 in different recycles.

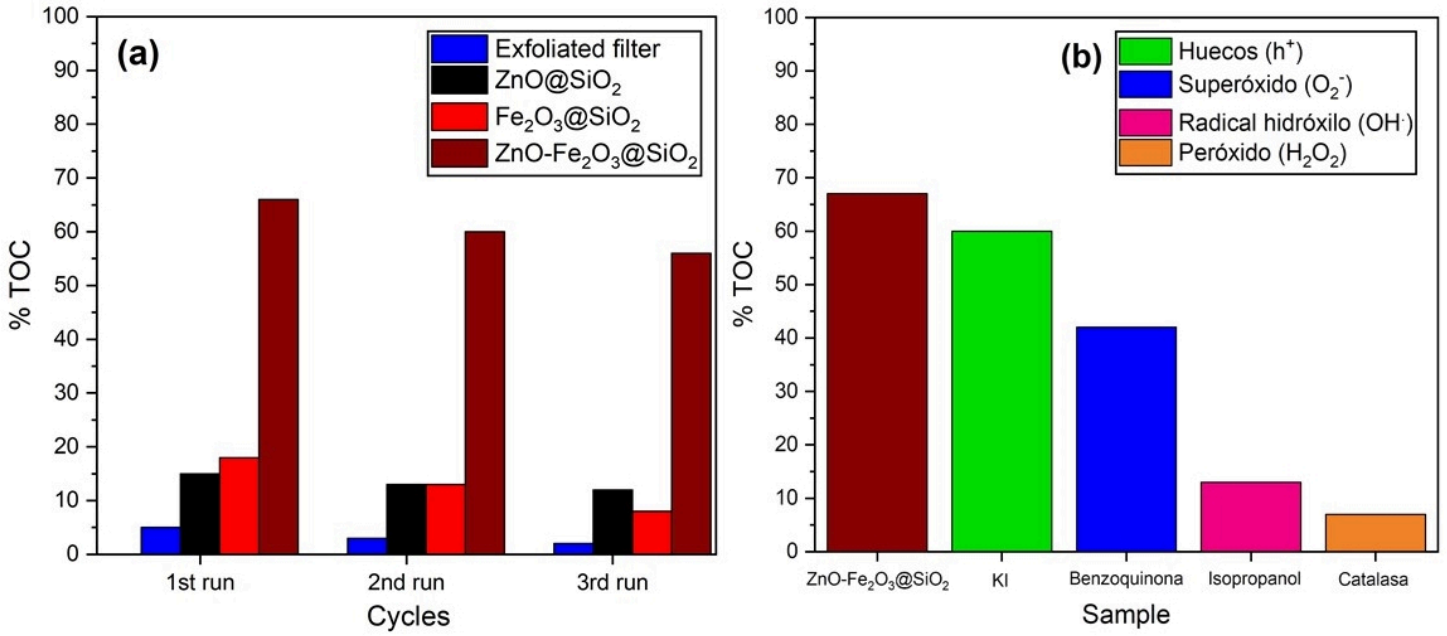


Figure 7

a) TOC analysis of monolithic filters in three reaction cycles; b) Scavenger effect on photocatalytic degradation of MB dye using ZnO-Fe_2O_3@SiO_2 filter.

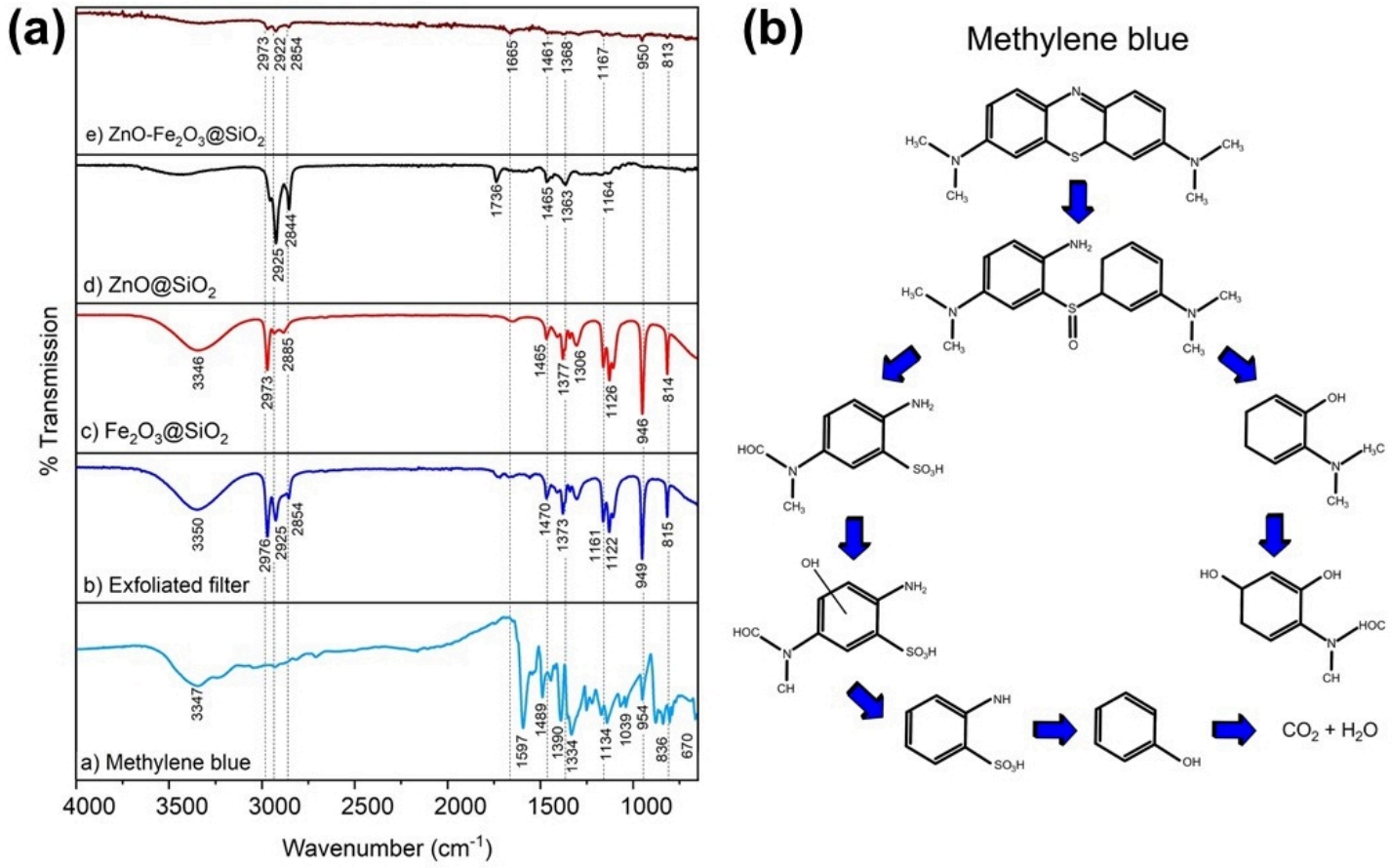


Figure 8

IR spectrum and reaction mechanism of methylene blue degradation by ZnO-Fe_2O_3@SiO_2 monolithic filters.